RMetS
Royal Meteorological Society

Structure of a shear-line polar low

D. E. Sergeev,[a]* I. A. Renfrew,[a] T. Spengler[b] and S. R. Dorling[a,c]
[a]*School of Environmental Sciences, University of East Anglia, Norwich, UK*
[b]*Geophysical Institute, Bjerknes Centre for Climate Research, University of Bergen, Norway*
[c]*Weatherquest Ltd., University of East Anglia, Norwich, UK*

*Correspondence to: D. E. Sergeev, School of Environmental Sciences, Centre for Ocean and Atmospheric Sciences, University of East Anglia, Norwich Research Park, Norwich NR4 7TJ, UK. E-mail: d.sergeev@uea.ac.uk

During March 2013 a series of polar lows originated in a high-vorticity ($>10^{-3}\,s^{-1}$) shear zone that was associated with a prolonged marine cold-air outbreak over the Norwegian Sea. A detailed analysis of one shear-line polar low at the leading edge of the outbreak is presented using comprehensive observations from a well-instrumented aircraft, dropsondes, scatterometer and CloudSat data, and numerical modelling output from a convection-resolving configuration of the Met Office Unified Model. The maximum low-level wind gradient across the shear line was $25\,m\,s^{-1}$ over 50 km. High winds to the north and west were within the cold air mass and were associated with large surface turbulent heat fluxes and convective clouds. Low wind speeds to the south and east of the shear line were associated with low heat fluxes and a clear 'eye' in the polar low. Shear-line meso-gamma-scale instabilities merging into the polar low appeared important to its structure and development. The model captured the shear line and the polar low structure very well–in particular the strength of the horizontal shear and the mesoscale thermodynamic fields. The spatial structure of convective cloud bands around the polar low was simulated reasonably well, but the model significantly underestimated the liquid water content and height of the cloud layers compared to the observations. Shear-line polar lows are relatively common, however this case is arguably the first to be examined with a wide range of *in situ* and remote observations allied with numerical model output.

Key Words: polar low; shear line; Norwegian Sea; aircraft observations; CloudSat; Met Office Unified Model

Received 13 June 2016; Revised 19 August 2016; Accepted 23 August 2016; Published online in Wiley Online Library

1. Introduction

Myriads of mesoscale vortices emerge over the Norwegian Sea during the extended winter period (November–April) (Kolstad, 2011; Rojo *et al.*, 2015). The life cycle of each of these vortices is uniquely shaped by its environment and by complex interactions between different physical processes such as baroclinic instability, latent heat release, and surface heat exchange. Under favourable conditions, some of these vortices gain sufficient energy to produce near-surface gale force winds and are referred to as polar lows (PLs)–some of the most extreme weather events of the high latitudes. With their intensity, they are a threat to coastal and maritime socio-economic activities (Hamilton, 2004). The chronic lack of *in situ* observations at high latitudes makes it challenging to forecast these small-scale and explosive weather phenomena accurately, even for modern numerical weather prediction (NWP) systems (Kristiansen *et al.*, 2011). This shortcoming is especially true at the early stages, when incipient perturbation PLs can be embedded in convergence zones with large horizontal wind shear. We present the evolution of such a shear-line PL using comprehensive observations obtained during the Aerosol–Cloud Coupling And Climate Interactions in the Arctic (ACCACIA) field campaign, in conjunction with satellite data and high-resolution model simulations performed with the UK Met Office's Unified Model (MetUM)–their operational NWP model.

Several modelling studies have focused on the dynamics of PLs over the Nordic Seas, e.g. Adakudlu and Barstad (2011), Nordeng and Røsting (2011) and Claud *et al.* (2004). To improve our theoretical concepts and to verify numerical models, it is necessary to gather detailed information about the anatomy and life cycles of archetypal PLs, ideally with high-quality airborne observations. However, aircraft field campaigns are expensive, with the additional impediment that it is difficult to have the aircraft in the right place at the right time to obtain the most useful observations. Consequently, less than a dozen PLs have been investigated by research aircraft.

The classic case-study by Shapiro *et al.* (1987) of a Norwegian Sea PL provides a vivid picture of a meso-alpha-scale vortex with well-defined mesoscale fronts and strong winds. Using data from

© 2016 The Authors. *Quarterly Journal of the Royal Meteorological Society* published by John Wiley & Sons Ltd on behalf of the Royal Meteorological Society.
This is an open access article under the terms of the Creative Commons Attribution License, which permits use, distribution and reproduction in any medium, provided the original work is properly cited.

an extensive range of observations, they conclude this PL was induced by a propagating upper-level trough and intensified due to baroclinic instability and convection. The wind speeds exceeded 30 m s^{-1} and were observed below 2 km at a radius of 100 km, with relative vorticity above 2×10^{-3} s^{-1}, representing the 'truly mesoscale' nature of the PL. Subsequent studies report similar PL structures with diameters typically in the range 300–700 km and maximum wind speeds usually above 20–25 m s^{-1} (e.g. Douglas and Shapiro, 1995; Brümmer *et al.*, 2009; Føre *et al.*, 2011). Estimated latent and sensible heat fluxes range between 200 and 500 W m^{-2} with the Bowen Ratio close to unity.

Modern aircraft observations of PLs can be substantially complemented by airborne lidar. For example, Wagner *et al.* (2011) used two lidars, including a Doppler wind lidar, to provide high-resolution cross-sections of water-vapour mixing ratio, backscatter ratio, and horizontal wind speeds through the inner part of a PL. These observations provide a very thorough description of a PL 'eye' and were essential to compare against the authors' axisymmetric and NWP models.

In the absence of *in situ* observations, satellites provide a sweeping source of observational data for PL detection and analysis, for instance through cloud imagery from the Advanced Very High Resolution Radiometer (AVHRR; Harold *et al.*, 1999). Ocean wind vectors from scatterometers are among the spaceborne data assimilated by forecasting centres (Chelton *et al.*, 2006). A few case-studies also pinpoint the benefits of using synthetic aperture radar (SAR) images to examine the fine-scale (resolution of 100–200 m) features of near-surface winds within PLs (Moore and Vachon, 2002; Furevik *et al.*, 2015). A new powerful tool to study the internal properties of PL clouds has become available with the launch of NASA's CloudSat in 2006. CloudSat measures radar reflectivity versus altitude in a nadir slice along the satellite track. Unlike hurricanes (Tourville *et al.*, 2015) and midlatitude cyclones (Field *et al.*, 2011), to the authors' knowledge there are no detailed PL investigations based on CloudSat data except for a short note by Forsythe and Haynes (2015), who briefly illustrate CloudSat's intersection of a PL that developed over the Labrador Sea in November 2013.

There were multiple PL events around the Svalbard archipelago during the ACCACIA intensive observational period in March–April 2013, and one of the most intense was investigated by our research aircraft on 26 March. The objective of this study is to scrutinise the structure of this PL, which developed along a shear line south of Svalbard. We focus specifically on the mesoscale features of the wind and temperature fields and on the cloud properties of the PL, assessing the liquid water and ice concentration at different levels. We use a wealth of observations, including direct measurements and dropsondes from the research aircraft, CloudSat radar data and MetOp-A's scatterometer products. In addition, the MetUM is run at convection-permitting 2.2 km grid spacing, in order to to deepen our analysis of the PL and validate this state-of-the-art operational model against the aforementioned observations. The choice of this PL is dictated by the uniqueness of the successful aircraft observations and their coincidence with appropriate satellite overpasses.

Sections 2 and 3 describe the observational data and the model set-up respectively. Section 4 presents the large-scale synoptic conditions before and during the PL development. Section 5 discusses the evolution of the PL and section 6 describes the mesoscale structure of the PL, while both evaluate the performance of the model. Section 7 synthesises and concludes this study.

2. Observational data

2.1. *Direct observations*

Our domain of interest is shown in Figure 1. Data were gathered by the BAe-146 aircraft of the Facility for Airborne Atmospheric Measurements (FAAM) during flight B763 on 26 March 2013. The on-board instruments provided standard meteorological variables, including the three components of wind velocity, pressure, temperature, and humidity (e.g. Renfrew *et al.*, 2008). Cloud droplet and ice crystal concentrations were sampled by the Cloud Droplet Probe (CDP) and the Two-Dimensional

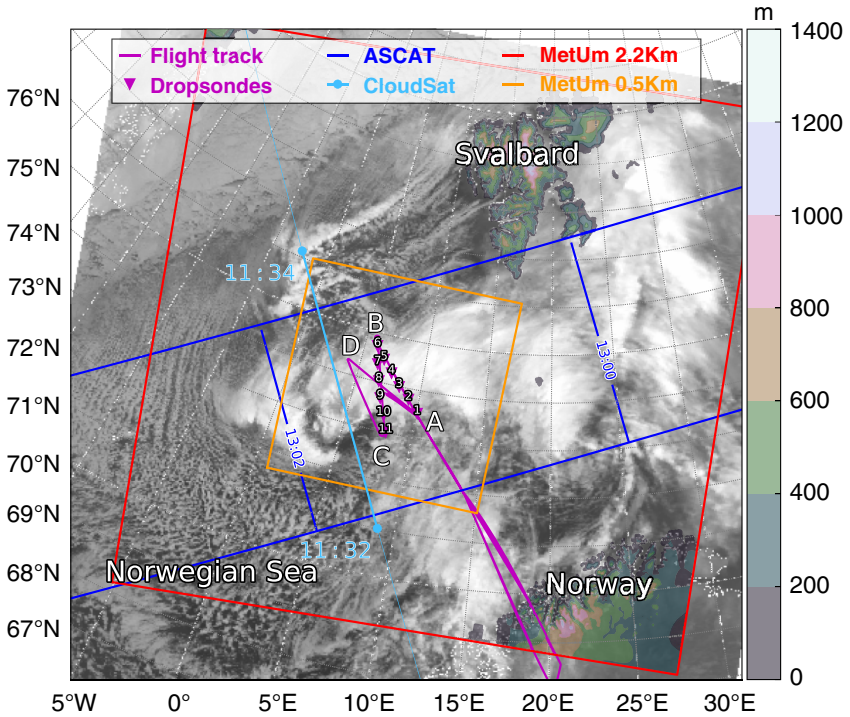

Figure 1. Observational and modelling domains. Cloud cover is shown as AVHRR channel 4 image (1220 UTC 26 March 2013). The modelling domains with 2.2 and 0.5 km grid spacing are marked by the red and orange boxes, respectively. The flight track (1016–1405 UTC) is shown by the purple line and dropsonde locations are marked as numbered triangles. The CloudSat (cyan) and ASCAT (blue) swaths are also overlaid. Model topography is shaded (m). [Colour figure can be viewed at wileyonlinelibrary.com].

© 2016 The Authors. *Quarterly Journal of the Royal Meteorological Society* published by John Wiley & Sons Ltd on behalf of the Royal Meteorological Society.

Stereoscopic Probe (2D-S) respectively; both are optical scattering probes. The particles were categorised by size and shape, and their number densities were converted to liquid (LWC) and ice water content (IWC). In addition, estimates of LWC and total (ice plus liquid) water content (TWC) were provided by the hot-wire deep cone Nevzorov probe (Korolev *et al.*, 1998). For convenience, all aircraft measurements are shown at 1 Hz resolution, which corresponds to a resolution of ≈100 m in the horizontal.

In addition, 11 GPS dropsondes (Vaisala RD93) were released sequentially every ≈5 min to obtain the vertical structure of the atmosphere. With typical terminal velocities of about 10 m s^{-1} (Petersen *et al.*, 2009), they provide vertical profiles of wind speed and direction, pressure, temperature, and humidity.

The B763 flight took place in the northern part of the Norwegian Sea, approximately within the area of 4–10°E, 73–75°N with the flight track following a 'butterfly' pattern (A–B–C–D–A). The period of measurements lasted from 1100 to 1400 UTC. Two legs (A–B, B–C) were made at an altitude of ≈6000 m above sea level (asl) when the dropsondes were released and their data sent to the Global Telecommunication System (GTS). The descent from C to D gave information about clouds on the northern side of the PL. The low-level quasi-horizontal run from D to A (with partial legs from A back towards D) was mainly at 35 m asl to allow estimates of surface layer characteristics. However, due to low visibility, the aircraft ascended to 300 m asl for 15 min. The mission finished with an ascending profile, in calm conditions close to point A. Overall, the flight was successful as both sides of the shear line were probed with profiles and legs at several altitudes.

2.2. *Satellite data*

Satellite remote-sensing instruments provide estimates of cloud composition, surface winds, and radiative fluxes.

Near-surface wind speed was obtained by the Advanced Scatterometer (ASCAT) installed on the polar-orbiting MetOp-A satellite. The dataset used in this study has 12.5 km resolution and covers the ocean surface in two 550 km-wide swaths. The applicability of ASCAT data to PL studies is discussed by Zabolotskikh *et al.* (2013) and Furevik *et al.* (2015). Although the satellite orbit goes through the same high-latitude region several times a day, only a few of the overpasses fully captured the observed shear line. We will focus on the 1300 UTC overpass.

Another satellite product comprises snapshots of top-of-atmosphere outgoing long-wave radiation (TOA OLR) retrieved by NOAA's Advanced Very High Resolution Radiometer (AVHRR) instrument. Observations are made in the thermal infrared channel (10.3–11.3 μm) with 1.09 km spatial resolution and give an excellent overview of the cloud features associated with the cold-air outbreak (Figure 1).

Until recently, the vertical structure of high-latitude marine weather phenomena could only be sampled by direct airborne observations or, rarely, by a research vessel's radar (e.g. Shapiro *et al.*, 1987). With the advent of CloudSat, carrying a highly sensitive 94 Hz cloud profiling radar, it has become possible to dissect and study the internal structure of such phenomena more comprehensively. Being a polar-orbiting satellite with sun-synchronous orbit, CloudSat provides a good coverage of high-latitude regions. It repeats the same ground track every 16 days, meaning that the Norwegian Sea, for example, is probed on average 4 times per day. Fortunately, the CloudSat orbit passed exactly over the area of interest within the period of aircraft observations (around 1130 UTC), allowing us to complement the observational dataset with radar reflectivity and other derived quantities sampled at 240 m vertical resolution and with 1.4 × 1.7 km footprint size. The reflectivity is measured within a −30 to 40 dBZ range (Tourville *et al.*, 2015).

3. Numerical model

We use one of the latest versions (v. 10.2) of the UK Met Office's Unified Model (MetUM) in atmosphere-only mode for this study. The model has been used several times in previous PL studies (e.g. Bracegirdle and Gray, 2009; Irvine *et al.*, 2011). The basic equations of the model are described in Davies *et al.* (2005) and essentially represent the atmosphere as a deep non-hydrostatic fully compressible fluid. The equations are discretised on an Arakawa C-grid in the horizontal and a Charney–Phillips grid in the vertical. Recently, significant improvements to the numerical schemes have been implemented in the model's dynamical core, now referred to as 'ENDGame' (Wood *et al.*, 2014). Changes to the model's physics, amongst many, included a new orographic drag scheme, a corrected convection entrainment scheme, and revised turbulent mixing for stable, unstable, and shear-dominated boundary layers, which improves the representation of clouds in polar cold-air outbreaks (Brown *et al.*, 2008).

The MetUM cloud microphysics scheme is a single-moment three-phase representation based on Wilson and Ballard (1999), with the use of multiple sub-time stepping and extensive modifications (e.g. the particle size distribution is described in Abel and Boutle, 2012). The parametrization uses prognostic cloud water and rain mixing ratios for the liquid phase. For ice there is a prognostic variable that represents all ice in the grid box. Production or loss of cloud water, ice and rain is governed by such processes as condensation, evaporation autoconversion, accretion, droplet settling, freezing of droplets by ice nucleation, diffusional growth and riming. The maximum ice nucleation temperature was set to −10 °C. For the large-scale cloud, the Smith scheme was used, which depends on the diagnostic cloud fraction and condensate variables, based on a symmetric triangular PDF of subgrid variability. Table 1 shows key model specifications. More details of the MetUM can be found in Walters *et al.* (2014) and references therein.

A global MetUM simulation with N768 resolution (17 km) was initialized using the operational analysis and generated boundary conditions for a nested model (Nesting Suite version u-aa753). The horizontal grid spacing of the limited-area model was ≈2.2 km, while the time step was 60 s. The domain was centred at 74°N, 15°E to capture the movement of the shear line and the emerging PL, as well as the northerly cold-air outbreak flowing around the Svalbard archipelago (Figure 1). Surface boundary conditions for sea-ice and sea-surface temperature were derived from the Operational Sea Surface Temperature and Sea Ice Analysis (OSTIA) at 17 km resolution and automatically downscaled to the nested model resolution.

We tested the impact of the initialization time, starting the simulations at 0600, 1200, 1800 UTC 25 March, and 0000 UTC 26 March. The majority of the analysis focuses on the midday conditions on 26 March. An additional experiment was performed

Table 1. MetUM control configuration.

Category	Specification
Dynamical core	Fully compressible non-hydrostatic Navier–Stokes equations
Advection scheme	Semi-implicit, semi-Lagrangian predictor–corrector scheme
Cartographic projection	Rotated pole
Horizontal grid spacing	2.2 km
Horizontal domain	1300 × 1300 km
Vertical grid	70 levels, including 16 levels below 1 km
Time step	60 s
Turbulence closure	Unstable conditions: non-local closure with entrainment fluxes Stable conditions: SHARPEST scheme
Microphysics	Single-moment 3-phase
Convection	Explicit

© 2016 The Authors. *Quarterly Journal of the Royal Meteorological Society* published by John Wiley & Sons Ltd on behalf of the Royal Meteorological Society.

with even smaller horizontal grid size (0.5 km) for the central part of the coarse-resolution domain (orange box in Figure 1).

The model output frequency was set to 10 min during the aircraft observations period and to one hour for the remaining time. All variables were interpolated to the middle points of grid boxes, to avoid problems with data analysis on the staggered grid. We use the Python packages Iris (Met Office, 2016) and Matplotlib (Droettboom *et al.*, 2016) for analysis and visualisation. All the code used in this study is publicly available on GitHub: https://github.com/dennissergeev/structure-of-a-shear-line-polar-low-notebooks (accessed 28 September 2016).

4. Synoptic overview

To understand the background state of the atmosphere prior to and during the PL event, we examined the 6-hourly ECMWF ERA-Interim reanalysis. Although there are notable constraints on how accurately PLs are represented in this dataset (Zappa *et al.*, 2014; Laffineur *et al.*, 2014), its purpose here is to give a general picture of the large-scale circulation over the North Atlantic. At the end of March 2013, polar maritime air masses over the western part of the Norwegian Sea were swept away by colder Arctic air during an intense cold-air outbreak. An upper-level ridge shifted southwestwards, and the study area began to be dominated by a cold trough, which stretched from the eastern Barents Sea with core temperatures below −45 °C (Figure 2(a)). By the time of the PL event, the temperature at 500 hPa had fallen by ≈8 K over the Norwegian Sea. Upper-level forcing appears important due to a large potential vorticity (PV) anomaly on the 285 K isentropic surface (not shown). The PV maximum reached values of 4–4.5 PVU and was located to the north (upstream) of the developing PL.

The 850 hPa thermal field reveals an intensification of the baroclinic zone (Figure 2(c, d)). Shaped by the cold-air outbreak to the west and warm sector advection to the east, it spreads all the way from Iceland to the eastern coast of Svalbard, and its orientation slowly became more meridional. The northern part of the baroclinic zone was characterized by a vertical velocity dipole with maximum amplitude at the height of 700 hPa, about 5° to the east of the observed PL position (not shown).

In the lower troposphere, a stationary large-scale depression prevailed over the area of interest, as shown by 850 hPa geopotential height (Figure 2(d)) and also evident in the mean-sea-level pressure (MSLP) simulated by the MetUM (Figure 3(a, c, e)). The synoptic depression slowly deepened, and the cloud bands of several mesoscale vortices can be clearly

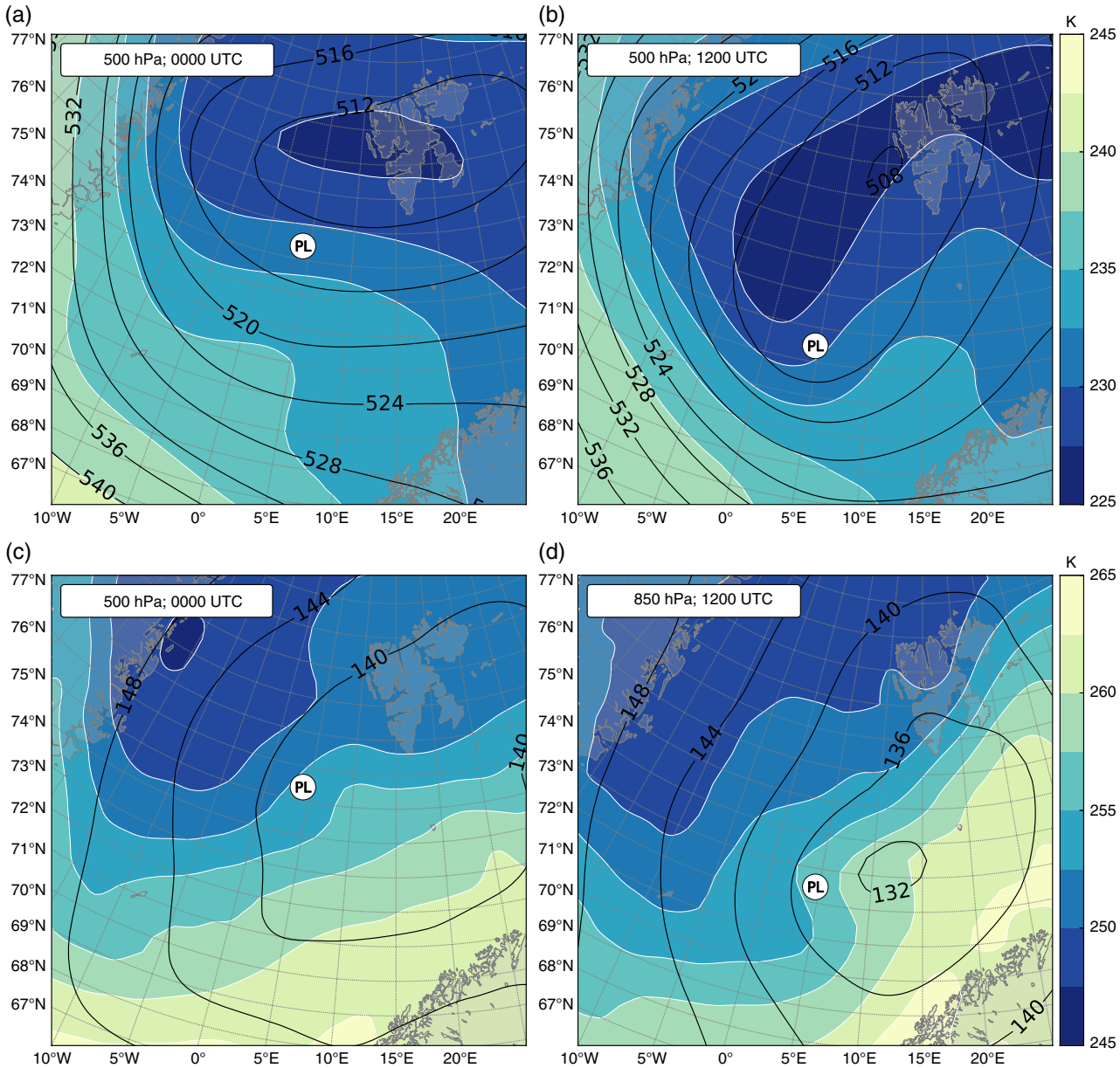

Figure 2. ERA-Interim air temperature (colour shading, K) and geopotential height (contours, ×10 m) at (a, b) 500 hPa and (c, d) 850 hPa for (a, c) 0000 UTC and (b, d) 1200 UTC 26 March 2013. The location of the PL (from subjective satellite analysis) in marked.

© 2016 The Authors. *Quarterly Journal of the Royal Meteorological Society* published by John Wiley & Sons Ltd on behalf of the Royal Meteorological Society.

distinguished on its periphery, including the one that was probed by the aircraft (Figures 1 and 3(e)). Originating in the cold-air outbreak in the rear part of the synoptic low, the vortices were steered by the cyclonic flow and formed a typical 'merry-go-round' pattern (Forbes and Lottes, 1985).

The cold-air outbreak appears in the cloud imagery as an area of shallow cellular convection, which again indicates significant surface–atmosphere temperature contrasts. In fact, the so-called marine cold-air outbreak (MCAO) index, which is proportional to the potential temperature difference between surface skin temperature and 700 hPa height (Bracegirdle and Kolstad, 2010), on 26 March was at its highest of the whole ACCACIA campaign period, implying that the observed PL developed during the strong advection of an Arctic air mass over the relatively warm

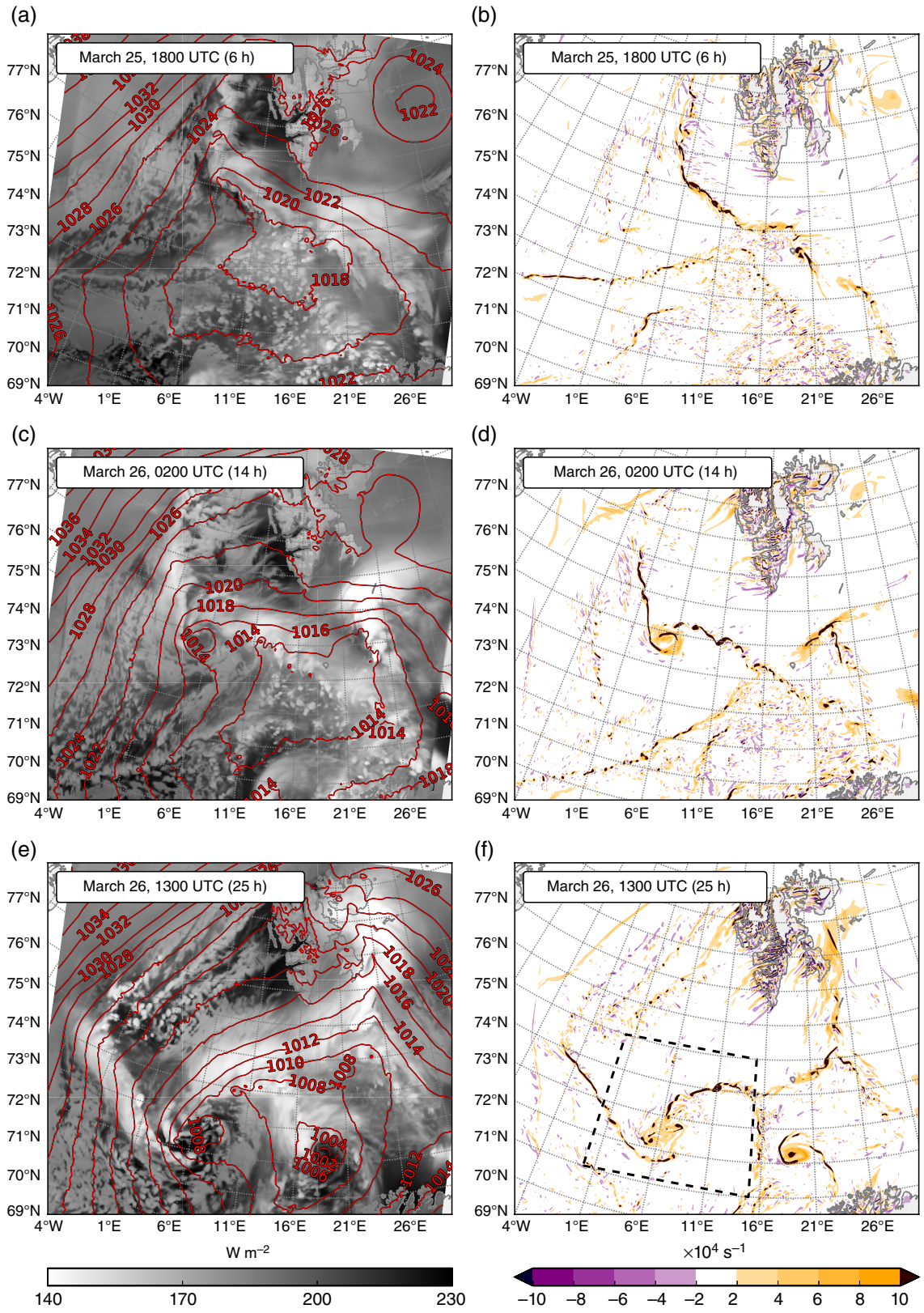

Figure 3. Temporal evolution of the PL shown by (a, c, e) simulated TOA OLR ($W\,m^{-2}$) with overlaid MSLP (red contours, hPa) and (b, d, f) relative vorticity ($\times 10^{-4}\,s^{-1}$) at 950 hPa for (a, b) 25 March 1800 UTC, (c, d) 26 March 0200 UTC, and (e, f) 26 March 1300 UTC. The dashed box in (f) displays the close-up area shown in Figures 4 and 8.

© 2016 The Authors. *Quarterly Journal of the Royal Meteorological Society* published by John Wiley & Sons Ltd on behalf of the Royal Meteorological Society.

ocean surface. These conditions often result in PL propagation being opposite to the thermal wind, i.e. reverse shear conditions (Terpstra *et al.*, 2016).

Given the outlined synoptic conditions, it is not surprising that PLs developed. The observed PL of interest started to grow on a convergence line (a trough in the MSLP field, Figure 3(a)) in the lee of Svalbard. The convergence line, discernible in the relative vorticity field (Figure 3(b, d, f)) at the leading edge of the trough, folded into the PL of interest and spawned chains of mesoscale waves along the northwest and northeast shear lines (section 5.2). In the satellite image at 1220 UTC (Figure 1), when the PL was centred at 73°N, 5°E, it can be pinpointed as a beak-like signature of bright (and hence, deep convective) cloud bands. The large-scale circulation during the PL event is common in this region: for example, the PL of 3–4 March 2008 developed in a similar background (Kristjánsson *et al.*, 2011).

5. Polar low simulation

Several model experiments have been conducted before the analysis of the weather phenomenon in detail. The set of experiments with 2.2 km grid spacing simulates the flow evolution skilfully, even with the default parametrization settings, usually applied for operational NWP over the British Isles. We carry out the MetUM validation primarily for wind velocity (u and v components), air temperature (T), air pressure (p), specific humidity, LWC and IWC, as well as sea-surface temperature (SST), and surface sensible (SHF) and latent (LHF) heat fluxes.

5.1. Sensitivity to grid spacing and initialisation time

Perhaps for the first time, a PL was simulated using a horizontal grid size of 0.5 km. The corresponding domain (500 × 500 km in size) was nested within the 2.2 km domain (Figure 1). Despite a finer representation of discrete convective cells, a qualitative comparison of wind speed and surface pressure revealed that this reduction in grid spacing did not give a remarkable improvement in model performance. This finding agrees with McInnes *et al.* (2011) for the same numerical model, who found that going from 12 km to 4 km in horizontal spacing led to considerably better results, while going further to 1 km was less fruitful.

Forecasting such rapidly evolving PLs is known to be sensitive to the numerical model's initialization time (Irvine *et al.*, 2011). Comparing the satellite data with the modelled total cloud amount, we noticed that the model reproduces the cloud patterns accurately both when initialized at 0000 UTC 26 March or 12 h earlier (not shown). On the other hand, the cloud bands surrounding the PL eye in the forecast from 0000 UTC mismatch reality as observed by AVHRR and the 1200 UTC 25 March simulation, e.g. the cloud-free gap between the two main cloud bands is missing in the 0000 UTC forecast (Figures 1 and 3(e)). In terms of MSLP, the PL minimum is slightly deeper in the later forecast (0000 UTC), leading to a stronger pressure gradient and higher than observed wind speeds. In longer lead-time simulations, the model skill deteriorates significantly, e.g. in the experiment starting at 0600 UTC 25 March, the wind maximum has a different shape and is located quite far from the observed shear line (not shown).

The initialization time experiments expose a degree of sensitivity in the location and shape of the shear line. The simulation initialized at 1200 UTC 25 March best matches the observations, particularly of low-level winds. This lead time (≈24 h) is probably not significant, as the size of the limited-area domain was a factor, as well as the atmospheric state at initialization time.

To sum up, the forecast run starting at 1200 UTC 25 March was chosen as the control experiment, as it qualitatively resembled the observations best, and thus was used for the further analysis of the internal structure of the PL.

5.2. Life cycle of the polar low

The results of high-resolution numerical experiments in conjunction with satellite imagery provide the opportunity to scrutinise the PL development in great detail. On 25 March, the northeasterly flow of the cold-air outbreak from the Barents Sea converged with the main branch of the northerly flow, forming a high relative vorticity banner with maxima of order 10^{-3} s^{-1} (Figure 3(b)). The banner was oriented from north to southeast and had a silhouette resembling the Svalbard coastline, while almost the whole area of the Norwegian Sea was speckled with smaller vortical disturbances. Starting from 1800 UTC (forecast time 6 h), the positive vorticity band began to bend and undulate, generating mesoscale shear-instability waves. The most unstable of these developed into a quasi-axisymmetric cyclonic disturbance at 0200 UTC 26 March, at the forecast time of 14 h (Figure 3(d)). The vorticity band continued to roll up, and smaller waves merged into the dominant mesocyclone, increasing its radius and pressure deficit.

In the morning of 26 March, even though the associated cloud structures do not stand out in the satellite imagery, they are discernible in the simulated top-of-atmosphere outgoing long-wave radiation field, as well as in the surface pressure field (Figure 3(c)). Over the next 14 h, the mesocyclone steadily deepened, dominating the vorticity field and maintaining a cloud-free core (Figure 3(e, f)). At midday, the PL centre is clearly seen as a MSLP minimum (closed 1008 hPa isobar) and as a dark patch in the OLR field. The main cloud bands have relatively low OLR (≈140 W m^{-2}), highlighting deep convection, and concur with the high-vorticity banners. Further to the southeast, another band of shallow convection is located (grey colours in the satellite imagery). The simulated OLR generally corresponds very well with the AVHRR image (compare Figure 3(e) to Figure 1), as does the simulated surface wind and scatterometer data (section 6.1).

At this time (midday, 24 h of the simulation), another mesoscale cyclone developed on a similarly folding vorticity banner a few hundreds of kilometres from the continental coast (Figure 3(f)) and became deeper in MSLP than the observed PL (Figure 3(e)). The new vortex moved northward, creating a large spiral cloud band and developing a much deeper trough within its core. Meanwhile, the observed PL continued to travel southeastward following the large-scale cyclonic flow. The PL grew in diameter, deepened to ≈1000 hPa and formed a more spiraliform cloud signature, but soon started to disintegrate into smaller disturbances that are visible both in the real and simulated cloud imagery (not shown). These disturbances filled the inner region of the PL, which can no longer be identified by a clear eye. Eventually the PL ceased to exist as a separate vortex and its remnants were absorbed into the new, stronger cyclone.

6. Mesoscale structures

The morphology of the shear-line PL is investigated via a combined analysis of aircraft flight-level observations, dropsonde profiles, ASCAT wind estimates, radar measurements from CloudSat and model results. The analysis here is confined to 1100–1400 UTC 26 March 2013. Note the PL translation velocity was about 10 m s^{-1} from the northwest at this time, subjectively determined from AVHRR imagery.

6.1. Horizontal structure

In the lower troposphere, the horizontal wind reached values of almost 25 m s^{-1} within the northeast shear line (Figure 4). The second shear line with wind speeds up to 10 m s^{-1} is related to northwesterly flow and separated from the former shear line by a thin trail corresponding to the cloudless gap seen in Figures 1 and 3(e). The scatterometer data generally confirm the model results, but the gradients are weaker than in the model and not

© 2016 The Authors. *Quarterly Journal of the Royal Meteorological Society* published by John Wiley & Sons Ltd on behalf of the Royal Meteorological Society.

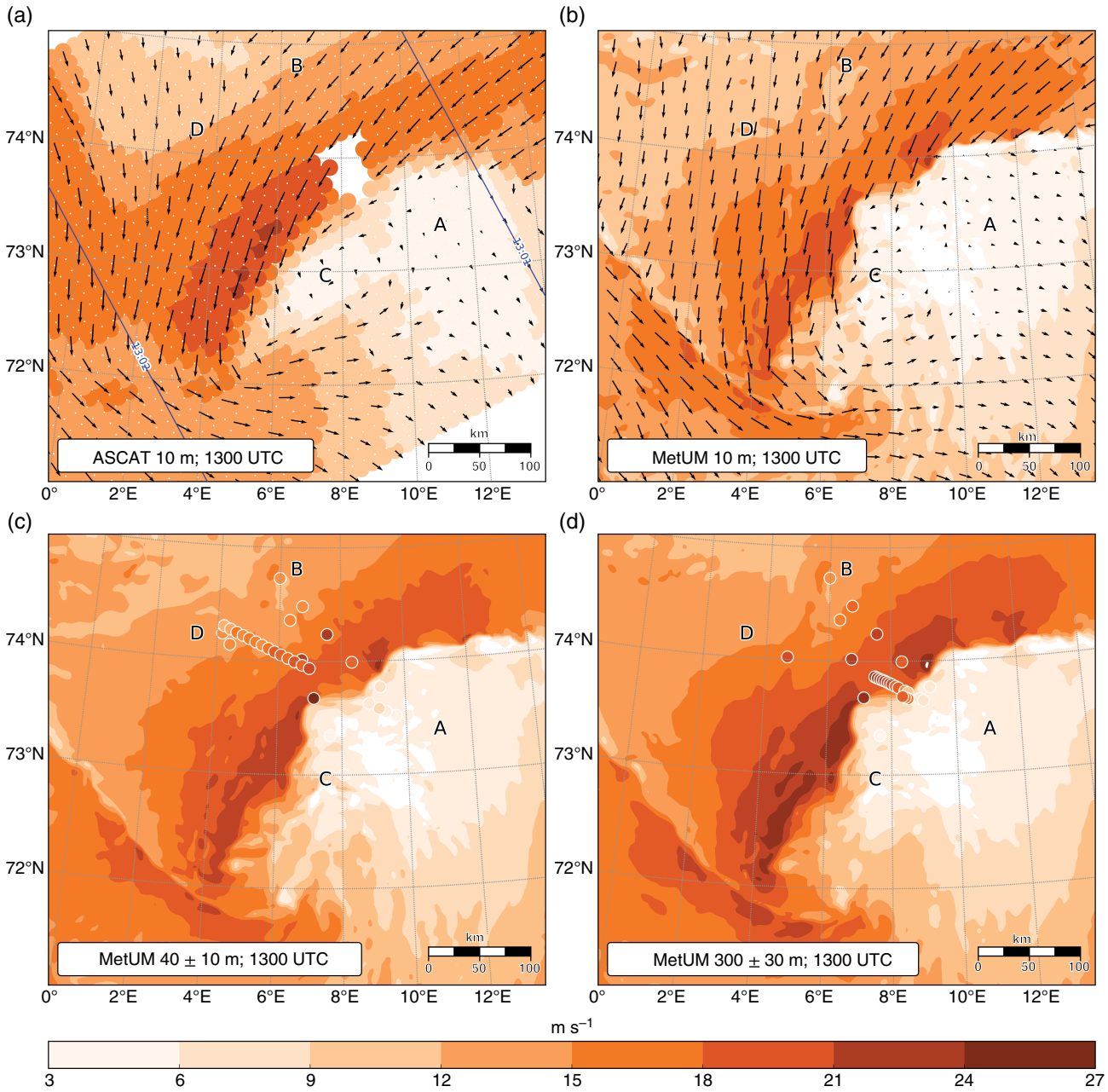

Figure 4. Surface wind magnitude ($m\,s^{-1}$) and direction (a) estimated by ASCAT and (b) simulated by MetUM. Wind speed from the model (colour shading) and airborne observations (coloured circles) at 1300 UTC (25 h of the simulation) are sampled and vertically averaged over (c) 40 ± 10 m, (d) 300 ± 30 m.

all the shear-line waves are well captured, most likely due to the relatively coarse spatial resolution (12.5 km). The northwest shear line and the convergence zone are less sharp in ASCAT data. Quantitatively, one can see the scatterometer's estimate is larger by 2–3 $m\,s^{-1}$, especially closer to the PL centre (Renfrew *et al.*, 2009). Finally, scatterometer retrievals do not provide a well-defined circulation centre in that region.

The horizontal wind structure is very similar at 300 m asl, but the magnitude is several $m\,s^{-1}$ higher than at 40 or 10 m (cf. Figure 4(b, c, d)). The PL core appears as an area of calm wind conditions, surrounded by shear lines. At this time its diameter is ≈100–150 km, so it can be classified as a meso-β-scale cyclone. In fact, the core of the PL consists of several small and weak vortices rotating around the main circulation axis (Figure 3(f)). Animations of the wind field suggest that shear instability waves feed the growing PL, while the vorticity source is concentrated upstream within the northeast shear line. The shear line is comprised of typically 5–6 meso-γ-scale undulations with wavelengths ranging from 20 to 100 km. With velocity exceeding 27 $m\,s^{-1}$, horizontal gradients are sharper across the shear line than within the PL core.

One of the most active 'wavy' parts of the northeast shear line was the area of our airborne observations, which are illustrated in Figure 4(c, d) by scattered circles. Note that the markers show not only the aircraft data sampled within the 40 ± 10 and 300 ± 30 m layer, but also the vertically averaged dropsonde measurements, although these are from 1.5 h earlier. Both levels demonstrate an excellent match between the numerical simulation and the observations in terms of the location, shape, and amplitude of shear instability waves.

6.2. *Vertical structure*

The shear line was penetrated several times during the research flight. The first two times occurred during high-altitude aircraft legs when the dropsondes were released (Figure 1), providing snapshots of the atmosphere below. As shown in Figure 5, the vertical cross-sections along the two flight legs, from southeast to northwest (A–B, (a, c)) and back to the southsoutheast (B–C, (b, d)), present the shear line as a zone with a very sharp wind speed gradient with a typical width of about 50 km, where the wind speed changes by more than 25 $m\,s^{-1}$, yielding a

© 2016 The Authors. *Quarterly Journal of the Royal Meteorological Society* published by John Wiley & Sons Ltd on behalf of the Royal Meteorological Society.

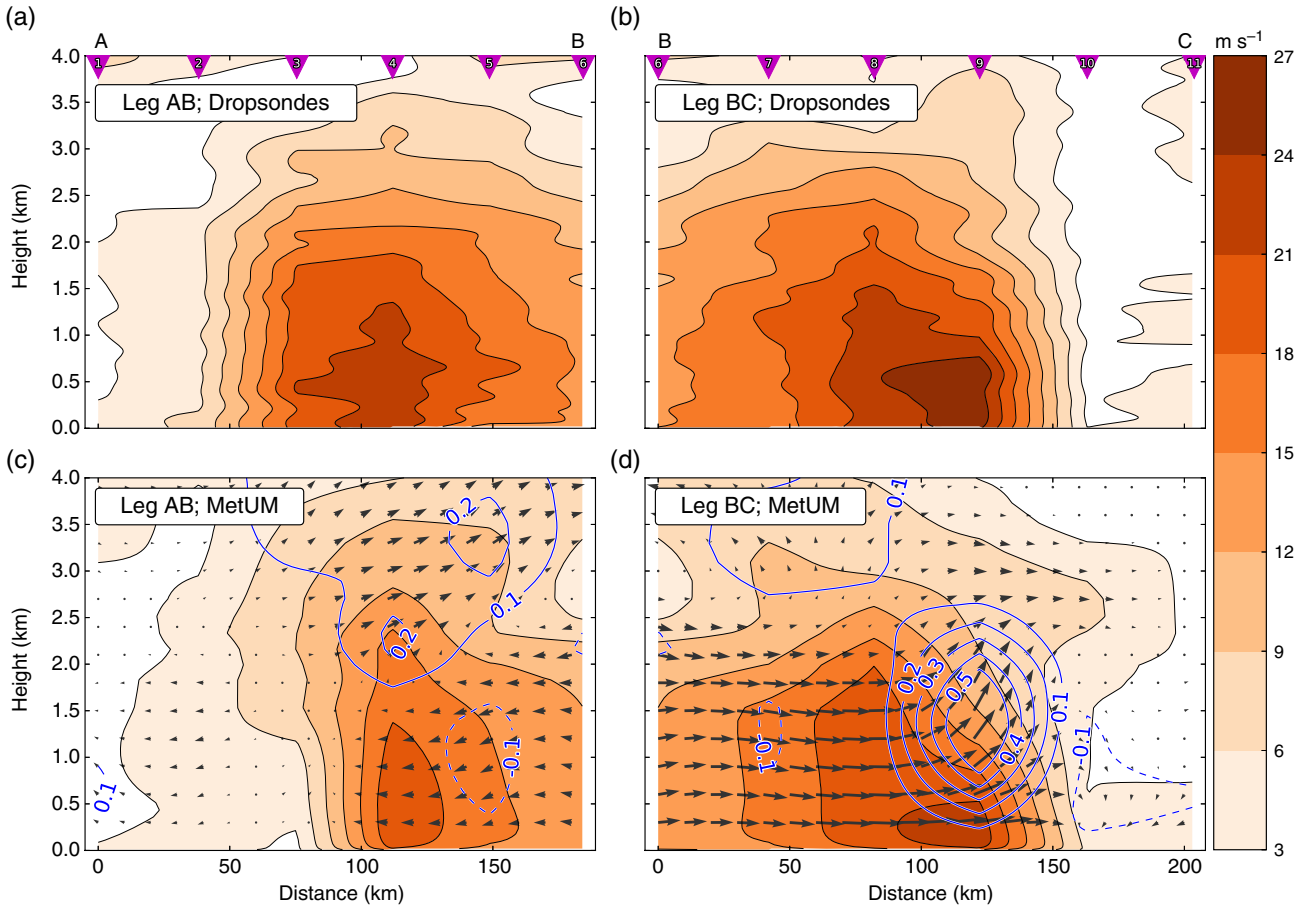

Figure 5. Vertical cross-sections of wind speed (colour shading, m s^{-1}) along the two flight legs across the shear line based on (a, b) interpolated dropsonde soundings and (c, d) model output. The simulated vertical velocity (blue contours, m s^{-1}) and tangential wind speed (black vectors) are overlaid on (c, d). Numbered triangles mark sounding locations. The dropsonde data in (a, b) were smoothed using a 25 s 6-order Butterworth filter.

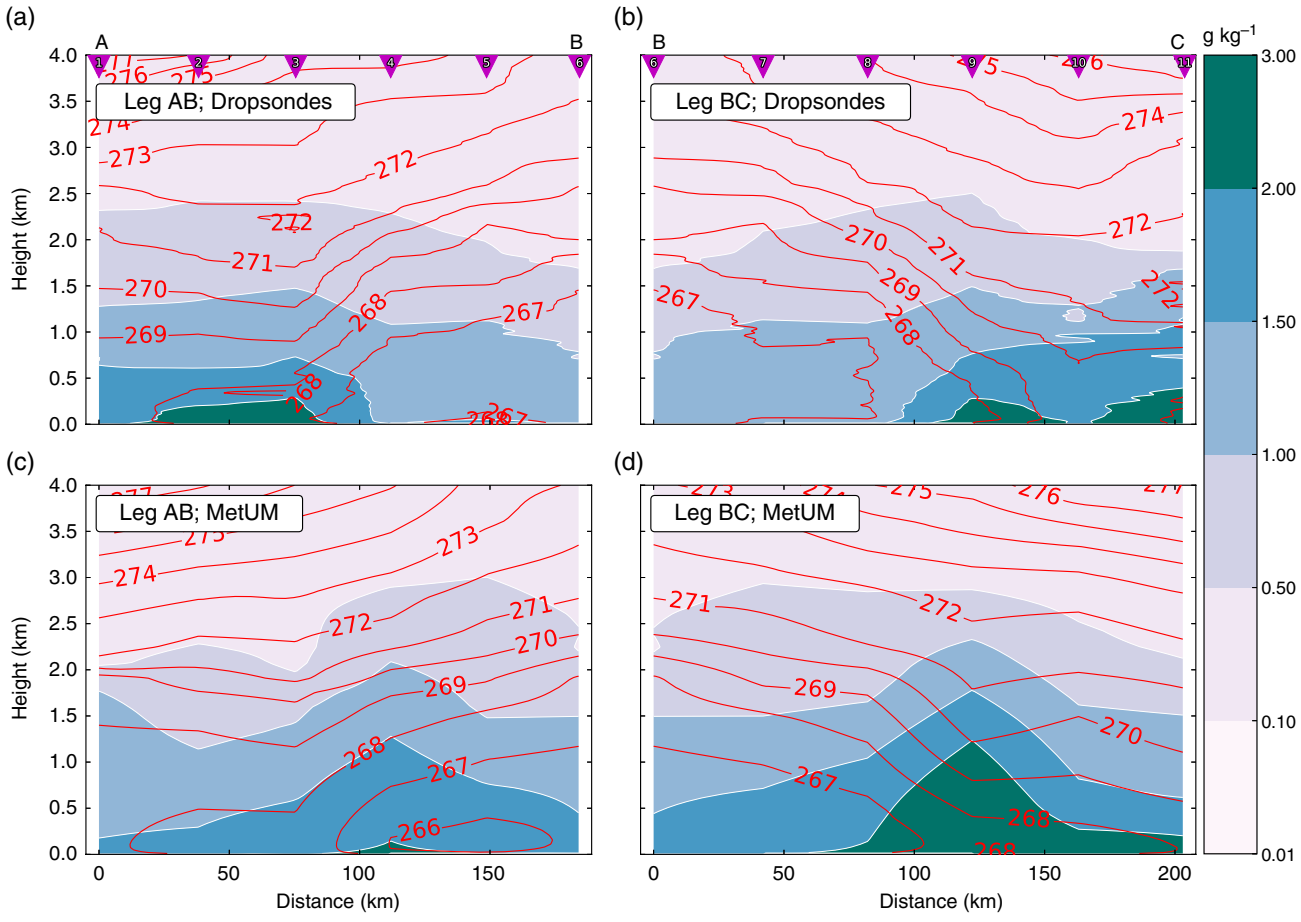

Figure 6. Vertical cross-sections of water vapour mixing ratio (log-scaled colour shading, g kg^{-1}) and potential temperature (red contours, K), as in Figure 5.

© 2016 The Authors. *Quarterly Journal of the Royal Meteorological Society* published by John Wiley & Sons Ltd on behalf of the Royal Meteorological Society.

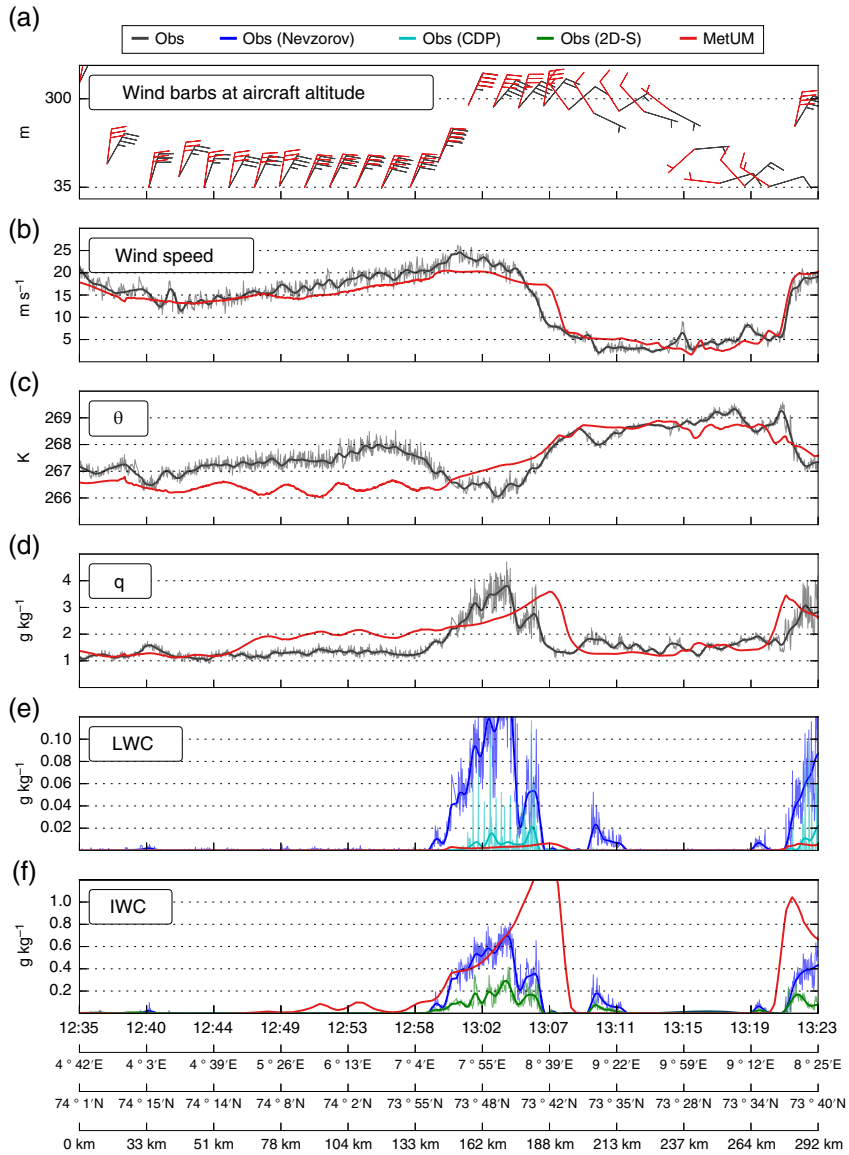

Figure 7. Time series of aircraft observations from low-level flight legs (D–A) and corresponding MetUM output: (a) wind speed and direction (barbs in standard meteorological notation) at aircraft altitude (m) measured by radar altimeter; (b) wind speed ($m\,s^{-1}$); (c) potential temperature (K); (d) total specific humidity ($g\,kg^{-1}$); (e) cloud LWC ($g\,kg^{-1}$) and (f) cloud IWC ($g\,kg^{-1}$). Thin curves show the original measurements, while thick curves show time series smoothed by 50 s 6-order Butterworth filter.

horizontal shear of $0.5\times10^{-3}\,s^{-1}$. The low-level jet is located to the northwest of the shear zone and was captured by dropsondes 4 and 9. The jet core is encircled by the $24\,m\,s^{-1}$ contour and is confined to the lowest 1000 m, while the horizontal shear remains large up to about 3000 m. Northward of the jet, the shear is not as strong, defining the forefront of the cold-air outbreak with steadily intense northerly flow. The overall correspondence between the observed and simulated winds is quite good. However, the simulated jet is slightly misplaced and more vertically constrained, while its magnitude is also lower by several $m\,s^{-1}$.

The shear line is evidently sharper along the B–C leg (Figure 5(b, d)), which traverses a crest of one of the instability waves (Figure 4(d)). Here, the low-level jet concurs with convection represented by high upward velocities in the model cross-section. Convective updraughts reach $0.55\,m\,s^{-1}$ and are concentrated precisely above the jet core, with a peak at 1500 m. The calm region to the south of the shear line has continuous downward motions with a minimum of $< -0.10\,m\,s^{-1}$ (along the B–C cross-section).

Two different boundary layers can be identified in the cross-sections of potential temperature and water vapour mixing ratio (Figure 6). The marine boundary layer of the warm air mass appears weakly stable and contains more moisture. Due to the high humidity, the vertical gradient of the equivalent potential temperature (θ_e, not shown) reveals that the boundary layer is conditionally neutral to ≈1500 m, while below 100–200 m there is a conditionally unstable surface layer. On the other hand, in the colder and drier Arctic air mass a neutrally stratified boundary layer develops to ≈1000 m, capped by enhanced stratification above. The isentropic surfaces slant at a relatively small angle with respect to the surface, forming a thermal front with a θ gradient of 3 K per 50 km in the lower 500–1000 m which appears to be in balance with the wind shear.

The MetUM skilfully reproduces the temperature field, with the exception of the very edge of the cold-air outbreak where the slope of isentropes is smoothed too much. In addition, the model makes the warm air too stable and colder than the *in situ* measurements. In terms of atmospheric moisture, the model over-amplifies the boundary-layer water vapour maximum at the shear line, which is linked with the strong LHF (next section) and coincident with high vertical velocity (Figure 5(d)) associated with strong convection. Quantitatively, our results are similar to those obtained for similar PL cases (Shapiro *et al.*, 1987; Brümmer *et al.*, 2009; Wagner *et al.*, 2011) where in the cloud bands near the PL core the water vapour mixing ratio is usually observed to be of the order of $2–3\,g\,kg^{-1}$. The θ_e field is also simulated well, though at the shear line, due to the overly humid air, the θ_e maximum is larger than in the dropsonde data.

© 2016 The Authors. *Quarterly Journal of the Royal Meteorological Society* published by John Wiley & Sons Ltd on behalf of the Royal Meteorological Society.

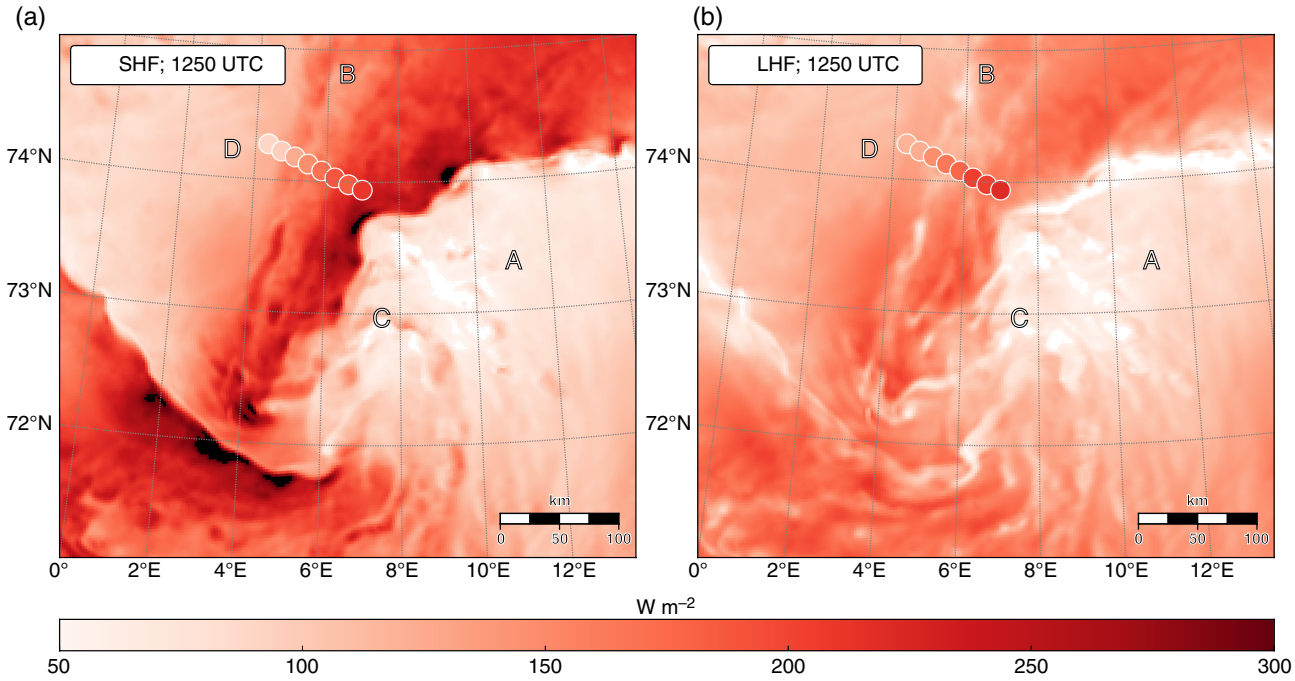

Figure 8. Surface (a) sensible and (b) latent heat flux (W m^{-2}) from the model (colour shading) and bulk flux estimates from the aircraft observations (coloured circles) at 1250 UTC.

6.3. *Surface layer characteristics*

The high-frequency data collected during the low-level flight legs (D–A) at ≈35 m asl allow us to study the shear zone boundary layer in great detail. The first part of the flight leg (1240–1258 UTC) took place within the cold-air outbreak, where the steady northnorthwesterly wind rose from 15 to 26 m s^{-1} towards the jet (Figure 7). The time series of potential temperature also indicates a gradual warming of the surface layer towards the shear line. At about 1300 UTC, the visibility severely worsened, and the aircraft had to climb to a higher altitude of ≈300 m asl for safety reasons. As evident in Figures 4 and 5, the boundary-layer wind field was well-mixed and the change in altitude does not affect the representation of the shear line greatly.

Corroborating the dropsonde data from an hour earlier, the horizontal shear line appears as a dramatic fall in wind speed over a distance of about 20–30 km. The atmospheric conditions within the shear zone are also characterized by a peak of water content. The specific humidity (Figure 7(d)), for instance, reaches 4–5 g kg^{-1}, while the ambient values for the surrounding air mass are 1–2 g kg^{-1}. The peaks in specific humidity, as well as in liquid water and ice particles (two bottom panels, respectively), are related to the shear-line cloud wall. The cloud base resides very close to the sea surface, as is evident in the peaks of cloud water content; cloud characteristics are presented in more detail in section 6.4.

In the tranquil zone southeast of the jet core (starting at 1307 UTC), wind speeds are 5 m s^{-1} or less; while the direction changes from northeasterly to southeasterly, a transition that is not well captured by the simulation. The near-surface measurements reveal cloud-free atmospheric conditions with higher potential temperature. The low-level boundary-layer stratification is close to neutral with $\theta = 268.5$ K, at least within the lowest 300 m.

After the aircraft descended, it took a U-turn to head northwestwards in the hope of probing the shear line again, but this time close to the sea surface. This accounts for the shear line appearing for the second time at the far right of Figure 7. This second encounter with the shear zone is valuable as it confirms the observations of the dramatic wind speed gradient, concomitant temperature gradient, and the cloud wall.

It is obvious that the MetUM capably reproduces the conditions within the surface layer in and around the shear zone, particularly the wind field, where the average error is only about 2 m s^{-1}, and the match in gradients is almost perfect. The structure of the temperature field is predicted with high skill, although the frontal zone in the model is steeper than in reality.

An intensive surface heat exchange is maintained by turbulent mixing underneath the strong low-level jet. Heat transfer from the ocean to the atmosphere exceeds 500 W m^{-2} and it is most intensive within the developing PL, where the wind speed also has the largest values. The SHF topped the LHF by at least a factor of 2 and reached ≈350 W m^{-2} (Figure 8). The SHF has two distinct maxima, one to the northwest of the observed shear line and the other one to the south of the second shear-dominated flank of the PL. The LHF is largest to the south of the PL, where the wind velocity is smaller, though the moisture deficit is larger. Along the northeast shear line, the LHF has values ≈220 W m^{-2}. Both the SHF and LHF patterns follow the northeast shear line waves (cf. Figure 4(d)).

The MetUM's representation of the boundary-layer fluxes is supported reasonably well by *in situ* observations. SHF and LHF were calculated along the 35 m flight legs from measurements of wind, temperature, water vapour mixing ratio, and radiometer measurements of SST using the COARE* 3.0 algorithm as well as the eddy-covariance technique (methodology is described in Cook and Renfrew, 2015). Only the bulk fluxes are shown here. The circles in Figure 8 show where the flux estimates were made at a flight altitude of 35 m and before the aircraft encountered the cloud wall of the shear line. Compared to the observations, the model overestimates the SHF by ≈30 W m^{-2}, a discrepancy which can be explained by a mismatch in temperature differences. Indeed, $\theta_{sea} - \theta_{air}$ temperatures are 2–3 K greater in the model than in observations. Scaled by the temperature difference factor only, the modelled values almost exactly match the observed ones. LHF, on the other hand, is underestimated by the MetUM by ≈65 W m^{-2} and this is most likely due to the overestimated values of specific humidity in the atmosphere (Figure 7). The absolute values of SHF and LHF stay roughly the same throughout the PL evolution and are close to some previous observational estimates

*Coupled Ocean–Atmosphere Response Experiment.

© 2016 The Authors. *Quarterly Journal of the Royal Meteorological Society* published by John Wiley & Sons Ltd on behalf of the Royal Meteorological Society.

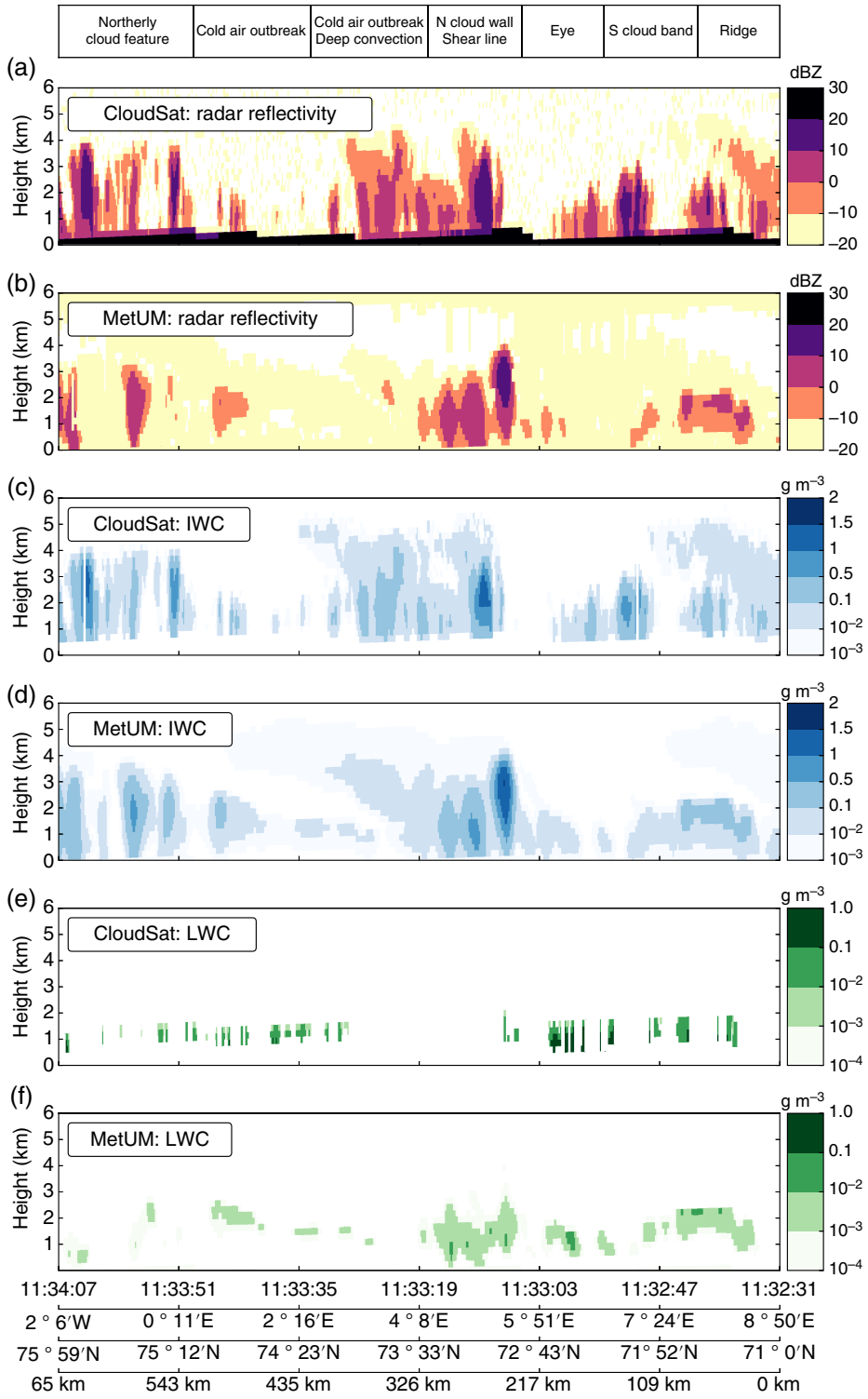

Figure 9. Cloud structure across the PL core region at 1130 UTC: (a) CloudSat radar reflectivity (dBZ); (b) MetUM radar reflectivity (dBZ); (c) CloudSat radar IWC density (g m^{-3}); (d) MetUM IWC density (g m^{-3}); (e) CloudSat radar LWC density (g m^{-3}) and (f) MetUM LWC density (g m^{-3}).

(Brümmer *et al.*, 2009; Føre *et al.*, 2011), but lower than others (Shapiro *et al.*, 1987; Wagner *et al.*, 2011).

6.4. *Cloud structure*

CloudSat measurements taken at around 1130 UTC elucidate the large-scale vertical cloud structure across the shear line and close to the PL centre. Radar reflectivity, as well as IWC and LWC are shown in Figure 9 and a corresponding cross-section from the MetUM simulation is given for each of these parameters. To obtain radar reflectivity, we used the Cloud Feedback Model Intercomparison Project Observation Simulator Package included in the MetUM (Bodas-Salcedo *et al.*, 2011). Note that the *x*-axes of Figure 9 are reversed so the plots run northwest to southeast.

The strongest radar echo (>20 dBZ) concurs with the shear line location, giving further evidence for the vigorous wall of clouds which the aircraft encountered carrying out low-level measurements (Figure 7). The high-reflectivity patch is identified as a cumulus-type cloud tower ≈4 km tall and ≈20 km wide, embedded in a conglomerate of shallow convective cells within the frontal part of the cold-air outbreak. The calm zone to the southeast, which can be labelled as a polar-low eye, is decently captured by the MetUM, although the location of individual clouds seems to be misplaced and underdeveloped. Large amounts of IWC are found within the cloud bands. In the

© 2016 The Authors. *Quarterly Journal of the Royal Meteorological Society* published by John Wiley & Sons Ltd on behalf of the Royal Meteorological Society.

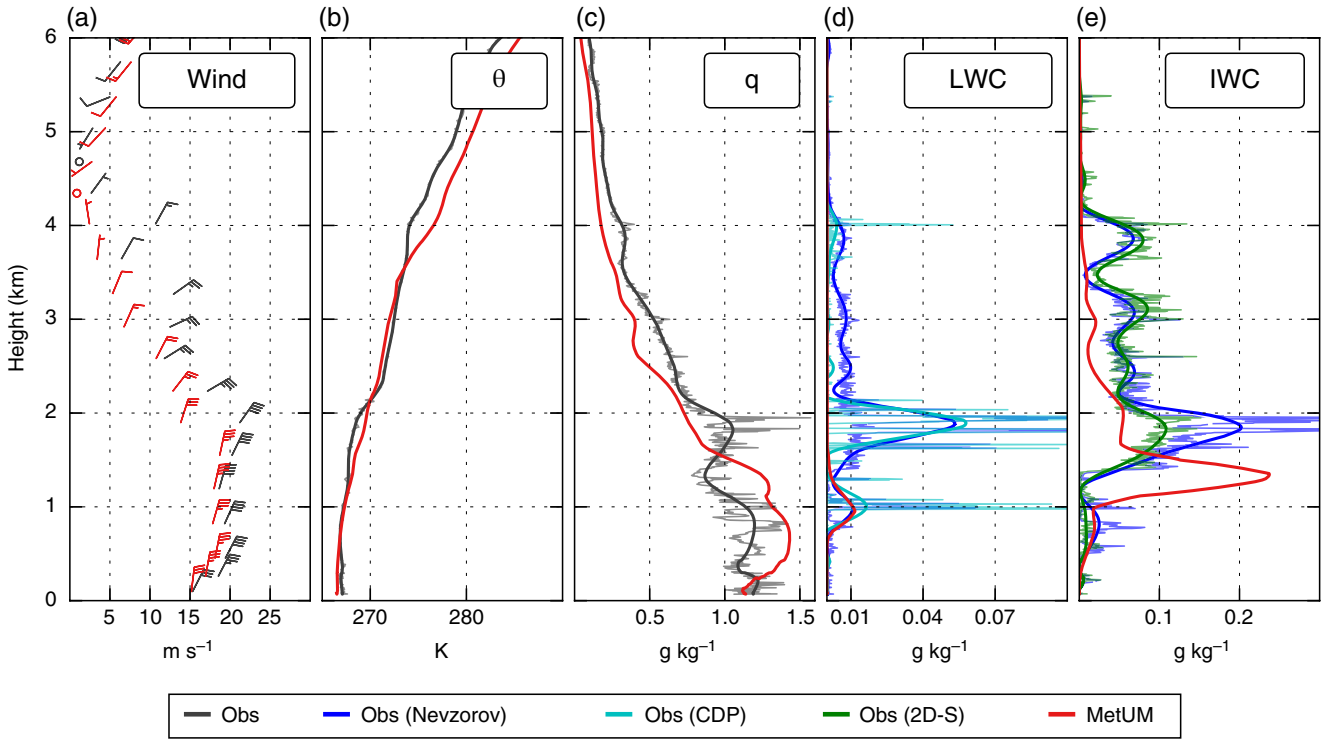

Figure 10. Time series of aircraft observations along the descending profile (C–D) and corresponding MetUM output: (a) wind speed and direction; (b) potential temperature (K); (c) total specific humidity ($g\,kg^{-1}$); (d) cloud LWC ($g\,kg^{-1}$) and (e) cloud IWC ($g\,kg^{-1}$).

shear-line cumuli, IWC reaches 1.0–1.5 $g\,m^{-3}$ at roughly 3 km height. The model has similar values but places the IWC peak ≈1 km too high. Underestimating the amount of ice crystals and water droplets in the southeast stratocumulus bands, the model contaminates the PL eye with low-level clouds mainly due to high IWC concentrations (Figure 9(d)). This substantiates the mismatch between the predicted and observed *in situ* values of specific humidity and LWC, shown in the bottom plots of Figure 7.

The CloudSat estimate of LWC is shown in Figure 9(e) in the same units but over a different range than for IWC. The liquid water is confined to the lowest 2 km and its concentration exceeds 1 $g\,m^{-3}$. The modelled LWC is more vertically spread than CloudSat records, and generally has lower values. The integral measurement of water content–liquid water path–is drastically mismatched. Ice water path, on the other hand, displays a better agreement, particularly in the shear-line region. In the northernmost segment of the track (left part of Figure 9(a)) CloudSat detected several bands of strong convection, which are visible in the AVHRR infrared imagery too (Figure 1). The presence of the convective bands indicates another region of instability due to the bending of a vorticity filament tail (Figure 3(f)) which grew upstream of the observed PL and was not well reproduced.

To further analyse the intricate structure of the cloud bands in the vicinity of the PL, we present the unique set of cloud microphysical equipment on board the FAAM aircraft (Figure 10; section. 2.1). These measurements were taken from ≈6 km to ≈40 m asl along the descending leg (C–D), when the aircraft was piercing the shear line in the southeast–northwest direction (1214–1238 UTC). A moist well-mixed subcloud layer is present up to about 600 m asl, followed firstly by tenuous layers of frozen water and then by a peak in liquid water at 1 km. The main cloud tower extends from 1.2 km up to the wind steering level at about 4.5 km, manifested by the IWC of at least 0.2 $g\,kg^{-1}$ (Figure 10(e)). The clouds are densest at ≈1.8–2 km, where both ice crystals and water droplets have maximum concentrations and which also contribute to the peak in total humidity (1.6 $g\,kg^{-1}$; Figure 10(c)).

The smoothed CDP and Nevzorov data consistently show that the LWC reaches 0.05 $g\,kg^{-1}$. Within the main cloud layer, the MetUM does not reproduce the increase in liquid droplets, but reproduces the IWC peak to a better degree, especially when compared to Nevzorov estimates, albeit placing it 500 m too low. Above 2 km, the cloud particle concentration is 2–3 times lower than the maximum, and the cloud consisted mostly of ice crystals. The LWC has a distinct 'lid' at a temperature of ≈ −20 °C, which is lower than reported in other ACCACIA flights (Lloyd *et al.*, 2015) and model studies (Field *et al.*, 2014a). This distinct top in LWC is also seen in the CloudSat data and to an extent in the MetUM (Figure 9(e, f)).

Overall, the clouds along the descending profile are characterized by the ratio of IWC and TWC fluctuating near 0.8, according to the Nevzorov probe. This demonstrates that the ice phase prevails over the liquid phase, although the cloud can be still categorized as mixed-phase (Korolev *et al.*, 2003). Meanwhile, the MetUM's IWC/TWC ratio stays around unity throughout the whole troposphere, only dropping to 0.6 within the lowest mixed-phase cloud layer at ≈1 km. It is worth noting that the CloudSat postprocessing algorithm appears to need some adjustment, because the IWC/TWC ratio is higher than that retrieved by the *in situ* observations.

The cloud structure of the shear line was measured twice during the horizontal flight legs, firstly at 300 m from southeast to northwest (1300 UTC, +1.5 h after CloudSat; Figure 7) and then at 860 m from northwest to southeast (1330 UTC, +2 h after CloudSat; Figure 11). Since the time gap between these legs is only ≈30 min, we can assume that the aircraft was in the same cloud band. Total specific humidity (q) exhibits a maximum of >3 $g\,kg^{-1}$ within the shear-line cloud wall and does not change significantly between the two legs. The cloud wall is associated with an increase in LWC: smoothed CDP data give 0.02 $g\,kg^{-1}$ at 300 m and almost 0.1 $g\,kg^{-1}$ at 860 m. The spatial distribution of liquid droplets is in a good agreement between CDP and the Nevzorov probes, although the latter tends to overestimate absolute values of LWC due to a residual effect of ice on the LWC sensor (Korolev *et al.*, 1998). This effect is likely to be at work during the descending profile (above 2 km) and during the

© 2016 The Authors. *Quarterly Journal of the Royal Meteorological Society* published by John Wiley & Sons Ltd on behalf of the Royal Meteorological Society.

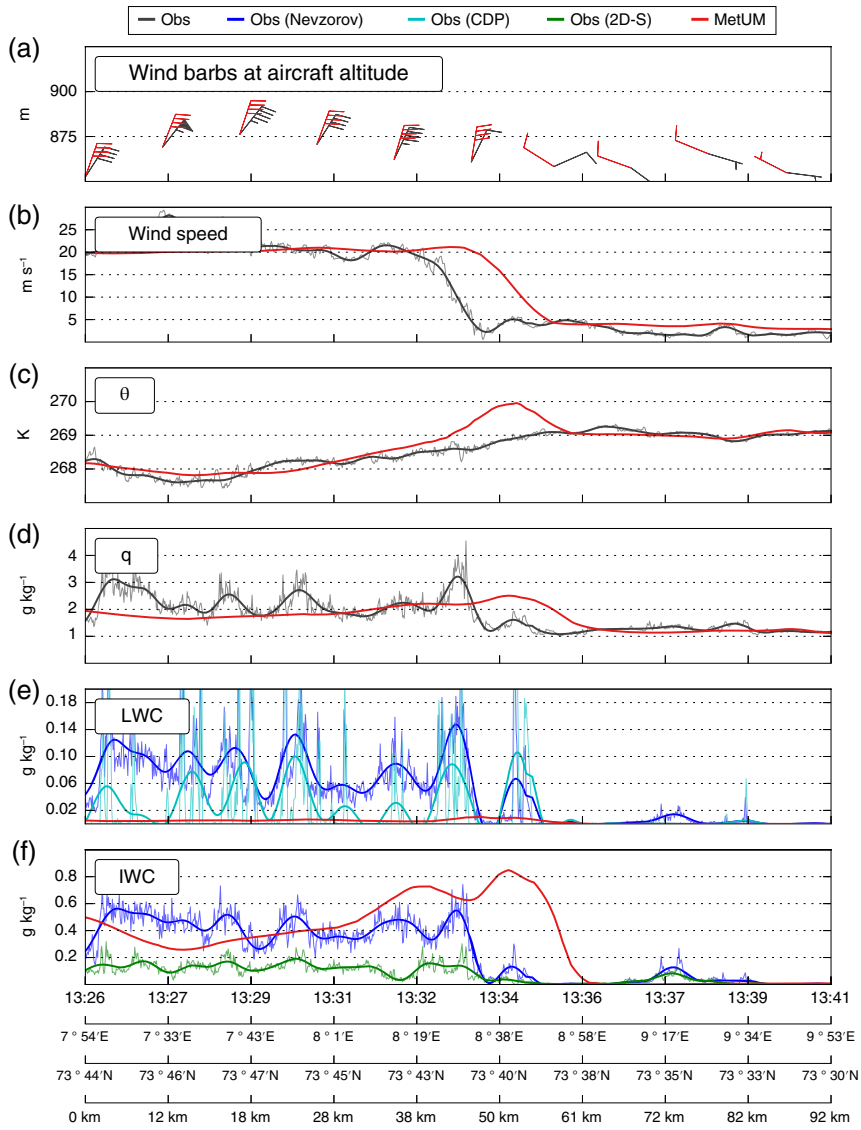

Figure 11. Time series of aircraft observations at about 860 m altitude and corresponding MetUM output, as Figure 7.

low-level flight (Figure 7(e)), where CDP shows little evidence of liquid phase particles; this is also close to the MetUM results.

The MetUM shows a prominent peak of IWC that collocates with the shear line and extends throughout the boundary layer, with values exceeding 1 g kg^{-1} (Figures 7 and 11). Nevertheless, the cloud wall is characterised by mixed-phase conditions. Within the cold air mass (within the first 50 km in Figure 11(e, f)), the clouds are weakly glaciated. There, the MetUM performs decently in representing the smoothed IWC time series. Although the 2D-S probe shows consistently lower estimates than the Nevzorov probe and the MetUM, the LWC is still substantially underestimated by the model, which also fails to accurately simulate several convective clouds to the northwest of the shear line, visible as peaks and troughs in water content a few kilometres in diameter. Recent investigations of mixed-phase cloud formation in turbulent environments suggested that changing one of the key parameters in the non-local boundary-layer scheme might be beneficial by allowing for disruption of cumulus formation through vertical wind shear (Field *et al.*, 2014b). However, in our sensitivity runs, the MetUM generated too many ice particles in one cloud layer, and too few in another, so the 'simple fix' of adjusting the boundary-layer parametrization seems dubious.

One of the most important findings revealed by the cloud analysis is the high intensity of convective cells in the forefront of the cold-air outbreak, indicating the importance of latent heat release in fuelling the PL. The radar echo pattern resembles that reported by Forsythe and Haynes (2015). In their brief note the reflectivity values also reach 20 dBZ within a cloud band of a Labrador Sea PL. The same values were reported by Kawashima and Fujiyoshi (2005), who studied meso-γ-scale snow bands over the Japan Sea using two Doppler radars. When compared to a tropical cyclone, PLs have similar radar reflectivity, but with maxima confined to the lowest 5 km (Tourville *et al.*, 2015).

7. Synthesis and conclusion

We examined the structure of a meso-β-scale shear-line PL which developed over the Norwegian Sea on 26 March 2013 using a combination of *in situ* and remote observations and convection-permitting numerical modelling.

In late March 2013, the synoptic situation was favourable for PL generation, with an intense marine cold-air outbreak bringing Arctic air masses over the relatively warm Norwegian Sea in the rear sector of a large-scale low. The northerly air streams were apparently deflected by the orography of the Svalbard archipelago, leading to convergence lines–vorticity bands–and the formation of mesoscale cyclones.

Broadly speaking, the observed PL was successfully simulated by the MetUM. The airborne observations demonstrate that the shear-line shape and magnitude were successfully captured. The ASCAT ocean wind vector estimates did not resolve the meso-γ-scale features, resulting in positive and negative wind speed biases. The dropsondes released across the shear line suggest that the horizontal shear zone was 3000 m deep and less

© 2016 The Authors. *Quarterly Journal of the Royal Meteorological Society* published by John Wiley & Sons Ltd on behalf of the Royal Meteorological Society.

than 50 km wide. The wind speed within the low-level jet reached 27 m s^{-1}, yielding relative vorticity of more than 10^{-3} s^{-1} along the shear line and near the PL centre. Similar values have been found in chains of mesocyclones over the Japan Sea (Nagata, 1993; Watanabe and Niino, 2014). The vertical cross-sections demonstrate a decrease of wind speed with height which is typical for a reverse-shear PL (Terpstra *et al.*, 2016). Representative of PL eye conditions, the cloud-free zone southeast of the shear line has relatively high temperatures (≈268 K), low wind speed (<5 m s^{-1}) and low total specific humidity (≈1.5 g kg^{-1}).

Analysis of the low-level aircraft measurements sheds light on the boundary-layer structure inside the cold-air outbreak. The atmosphere near the ocean surface appears to have a neutral to slightly unstable stratification. In the model, the surface layer is insufficiently mixed, leading to a 3 K error in the vertical difference of potential temperature, and consequently an overestimation of the SHF of roughly 30 W m^{-2}. The model also features too humid Arctic air, which results in an unduly low LHF. However, within the shear zone, θ is close to the observed values, and we expect the total turbulent heat exchange, exceeding 500 W m^{-2}, to be close to reality.

As far as cloud structure is concerned, the shear line is concomitant with a mixed-phase cloud band. The MetUM recreates the total humidity profiles reasonably well, but struggles to balance the ice crystal and water droplet concentrations, which is in accordance with the recent study of cold-air outbreaks by Field *et al.* (2014b). The clouds appear over-glaciated, suggesting the model is too efficient at removing liquid water: the simulated LWC is at least one order of magnitude smaller than that observed.

A novel approach presenting the PL structure via CloudSat data is used. Its radar provided a cloud profile across the shear line and the PL. Supporting the airborne observations, the shear line corresponded to intense convection with vertical velocity >0.5 m s^{-1} and radar reflectivity exceeding 20 dBZ. Both the MetUM and CloudSat reveal that the convective clouds around the PL centre are mostly mixed-phase below 2.5 km asl and glaciated above, where IWC reaches 1.5 g m^{-3}. The model does not fully reproduce the southern cloud wall of the PL, as well as some parts of the cold-air outbreak cloud bands. Overall, the CloudSat data were corroborated by the aircraft observations and proved to be useful in model verification–a great asset for PL research.

Further research is needed to understand the evolution and dynamics of this and similar shear-line PLs and their sensitivity to the upstream orography. In particular, future studies could aim to quantify contributions of different energy sources for the PL development. This might elucidate the role of barotropic instability within the vorticity filaments, which could be as important as convection and latent heat release.

Acknowledgements

We are greatly thankful to S. Webster, A. Elvidge and A. Orr for invaluable advice and technical assistance with the MetUM. We appreciate the help of A. Bodas-Salcedo in setting up the COSP model diagnostics. We thank S. Abel for guidance on using the cloud data. We acknowledge use of the MONSooN system, a collaborative facility supplied under the Joint Weather and Climate Research Programme, a strategic partnership between the Met Office and the Natural Environment Research Council. We also would like to thank all at the Facility for Airborne Atmospheric Measurements for the successful operation during the ACCACIA campaign and processing of the airborne data. Data from 2DS cloud probe are processed by the Centre for Atmospheric Science, University of Manchester, UK. CloudSat data were obtained from the CloudSat Data Processing Center (http://www.cloudsat.cira.colostate.edu; accessed 298 September 2016). AVHRR data were produced by the NEODAAS NERC Satellite Receiving Station, Dundee University, UK (http://www.sat.dundee.ac.uk; accessed 28 September 2016). ASCAT ocean wind vector data were downloaded from the NASA EOSDIS Physical Oceanography Distributed Active Archive Center at the Jet Propulsion Laboratory, USA (http://podaac.jpl.nasa.gov; accessed 28 September 2016). This work was made possible by funding provided by the Natural Environmental Research Council under grant NE/I028297/1 (ACCACIA). The first author was supported by a Lord Zuckerman scholarship at the School of Environmental Sciences, University of East Anglia. Partial funding for T. Spengler came from the University of Bergen Fund ID 7865 for his sabbatical in the United Kingdom and through the Research Council of Norway project HIMWARC (207875). We thank three reviewers, whose valuable comments have improved this article.

References

Abel SJ, Boutle IA. 2012. An improved representation of the raindrop size distribution for single-moment microphysics schemes. *Q. J. R. Meteorol. Soc.* **138**: 2151–2162.

Adakudlu M, Barstad I. 2011. Impacts of the ice-cover and sea-surface temperature on a polar low over the Nordic seas: A numerical case-study. *Q. J. R. Meteorol. Soc.* **137**: 1716–1730.

Bodas-Salcedo A, Webb MJ, Bony S, Chepfer H, Dufresne JL, Klein SA, Zhang Y, Marchand R, Haynes JM, Pincus R, John VO. 2011. COSP: Satellite simulation software for model assessment. *Bull. Am. Meteorol. Soc.* **92**: 1023–1043, doi: 10.1175/2011BAMS2856.1.

Bracegirdle TJ, Gray SL. 2009. The dynamics of a polar low assessed using potential vorticity inversion. *Q. J. R. Meteorol. Soc.* **893**: 880–893.

Bracegirdle TJ, Kolstad EW. 2010. Climatology and variability of Southern Hemisphere marine cold-air outbreaks. *Tellus A* **62**: 202–208, doi: 10.1111/j1600-08702009.00431.x.

Brown AR, Beare RJ, Edwards JM, Lock AP, Keogh SJ, Milton SF, Walters DN. 2008. Upgrades to the boundary-layer scheme in the Met Office numerical weather prediction model. *Boundary-Layer Meteorol.* **128**: 117–132, doi: 10.1007/s10546-008-9275-0.

Brümmer B, Müller G, Noer G. 2009. A polar low pair over the Norwegian Sea. *Mon. Weather Rev.* **137**: 2559–2575, doi: 10.1175/2009MWR2864.1.

Chelton DB, Freilich MH, Sienkiewicz JM, Von Ahn JM. 2006. On the use of QuikSCAT scatterometer measurements of surface winds for marine weather prediction. *Mon. Weather Rev.* **134**: 2055–2071.

Claud C, Heinemann G, Raustein E, McMurdie L. 2004. Polar low *le Cygne*: Satellite observations and numerical simulations. *Q. J. R. Meteorol. Soc.* **130**: 1075–1102.

Cook P, Renfrew IA. 2015. Aircraft-based observations of air–sea turbulent fluxes around the British Isles. *Q. J. R. Meteorol. Soc.* **141**: 139–152, doi: 10.1002/qj.2345.

Davies T, Cullen MJP, Malcolm AJ, Mawson MH, Staniforth A, White AA, Wood N. 2005. A new dynamical core for the Met Office's global and regional modelling of the atmosphere. *Q. J. R. Meteorol. Soc.* **131**: 1759–1782, doi: 10.1256/qj.04.101.

Douglas MW, Shapiro MA. 1995. Research aircraft observations of a polar low at the east Greenland ice edge. *Mon. Weather Rev.* **123**: 5–15.

Droettboom M, Hunter J, Caswell TA, Firing E, Nielsen JH, Elson P, Root B, Dale D, Lee JJ, Seppänen JK, McDougall D, Straw A, May R, Varoquaux N, Yu TS, Ma E, Moad C, Silvester S, Gohlke C, Würtz P, Hisch T, Ariza F, Cimarron C, Thomas I, Evans J, Ivanov P, Whitaker J, Hobson P, de Hoon M, Giuca M. 2016. 'matplotlib: matplotlib v1.5.1', doi: 10.5281/zenodo.44579.

Field PR, Bodas-Salcedo A. 2011. Using model analysis and satellite data to assess cloud and precipitation in midlatitude cyclones. *Q. J. R. Meteorol. Soc.* **137**: 1501–1515, doi: 10.1002/qj.858.

Field PR, Cotton RJ, McBeath K. 2014a. Improving a convection-permitting model simulation of a cold air outbreak. *Q. J. R. Meteorol. Soc.* **140**: 124–138, doi: 10.1002/qj.2116.

Field PR, Hill AA, Furtado K, Korolev A. 2014b. Mixed-phase clouds in a turbulent environment. Part 2: Analytic treatment. *Q. J. R. Meteorol. Soc.* **140**: 870–880, doi: 10.1002/qj.2177.

Forbes GS, Lottes WD. 1985. Classification of mesoscale vortices in polar airstreams and the influence of the large-scale environment on their evolutions. *Tellus A* **37A**: 132–155.

Føre I, Kristjánsson JE, Saetra Ø, Breivik Ø, Røsting B, Shapiro MA. 2011. The full life cycle of a polar low over the Norwegian Sea observed by three research aircraft flights. *Q. J. R. Meteorol. Soc.* **137**: 1659–1673, doi: 10.1002/qj.825.

Forsythe JM, Haynes JM. 2015. CloudSat observes a Labrador Sea polar low. *Bull. Am. Meteorol. Soc.* **96**: 1229–1231, doi: 10.1175/BAMS-D-14-00058.1.

Furevik BR, Schyberg H, Noer G, Tveter F, Röhrs J. 2015. ASAR and ASCAT in polar low situations. *J. Atmos. Oceanic Technol.* **32**: 783–792, doi: 10.1175/JTECH-D-14-00154.1.

Hamilton L. 2004. The polar low phenomenon. *GEO Q.* (1): 10–12.

Harold JM, Bigg GR, Turner J. 1999. Mesocyclone activity over the Northeast Atlantic. Part 1: Vortex distribution and variability. *Int. J. Climatol.*

© 2016 The Authors. *Quarterly Journal of the Royal Meteorological Society* published by John Wiley & Sons Ltd on behalf of the Royal Meteorological Society.

19: 1187–1204, doi: 10.1002/(SICI)1097-0088(199909)19:11<1187::AID-JOC419>3.0.CO;2-Q.

Irvine EA, Gray SL, Methven J. 2011. Targeted observations of a polar low in the Norwegian Sea. *Q. J. R. Meteorol. Soc.* **137**: 1688–1699.

Kawashima M, Fujiyoshi Y. 2005. Shear instability wave along a snowband: Instability structure, evolution, and energetics derived from dual-Doppler radar data. *J. Atmos. Sci.* **62**: 351–370, doi: 10.1175/JAS-3392.1.

Kolstad EW. 2011. A global climatology of favourable conditions for polar lows. *Q. J. R. Meteorol. Soc.* **137**: 1749–1761.

Korolev AV, Strapp JW, Isaac GA, Nevzorov AN. 1998. The Nevzorov airborne hot-wire LWC-TWC probe: Principle of operation and performance characteristics. *J. Atmos. Oceanic Technol.* **15**: 1495–1510, doi: 10.1175/1520-0426(1998)015<1495:Tnahwl>2.0.Co;2.

Korolev AV, Isaac GA, Cober SG, Strapp JW, Hallett J. 2003. Microphysical characterization of mixed-phase clouds. *Q. J. R. Meteorol. Soc.* **129**: 39–65, doi: 10.1256/qj.01.204.

Kristiansen J, Sørland SL, Iversen T, Bjørge D, Køltzow MO. 2011. High-resolution ensemble prediction of a polar low development. *Tellus A* **63**: 585–604.

Kristjánsson JE, Thorsteinsson S, Kolstad EW, Blechschmidt AM. 2011. Orographic influence of east Greenland on a polar low over the Denmark Strait. *Q. J. R. Meteorol. Soc.* **137**: 1773–1789, doi: 10.1002/qj.831.

Laffineur T, Claud C, Chaboureau JP, Noer G. 2014. Polar lows over the Nordic Seas: Improved representation in ERA-Interim compared to ERA-40 and the impact on downscaled simulations. *Mon. Weather Rev.* **142**: 2271–2289, doi: 10.1175/MWR-D-13-00171.1.

Lloyd G, Choularton TW, Bower KN, Crosier J, Jones H, Dorsey JR, Gallagher MW, Connolly P, Kirchgaessner ACR, Lachlan-Cope T. 2015. Observations and comparisons of cloud microphysical properties in spring and summertime Arctic stratocumulus clouds during the ACCACIA campaign. *Atmos. Chem. Phys.* **15**: 3719–3737, doi: 10.5194/acp-15-3719-2015.

McInnes H, Kristiansen J, Kristjánsson JE, Schyberg H. 2011. The role of horizontal resolution for polar low simulations. *Q. J. R. Meteorol. Soc.* **137**: 1674–1687, doi: 10.1002/qj.849.

Met Office. 2016. 'Iris v1.9.2 [Dataset]', doi: 10.5281/ zenodo.51860.

Moore GWK, Vachon PW. 2002. A polar low over The Labrador Sea: Interactions with topography and an upper-level potential vorticity anomaly, and an observation by RADARSAT-1 SAR. *Geophys. Res. Lett.* **29**: 20-1–20-4, doi: 10.1029/2001GL014007.

Nagata M. 1993. Meso-β-scale vortices developing along the Japan Sea polar airmass Convergence Zone (JPCZ) cloud band: Numerical simulation. *J. Meteorol. Soc. Jpn.* **71**: 43–57.

Nordeng T, Røsting B. 2011. A polar low named *Vera*: The use of potential vorticity diagnostics to assess its development. *Q. J. R. Meteorol. Soc.* **137**: 1790–1803.

Petersen GN, Renfrew IA, Moore GWK. 2009. An overview of barrier winds off southeastern Greenland during the Greenland Flow Distortion experiment. *Q. J. R. Meteorol. Soc.* **135**: 1950–1967, doi: 10.1002/qj.

Renfrew IA, Petersen GN, Outten S, Sproson D, Moore GWK, Hay C, Ohigashi T, Zhang S, Kristjánsson JE, Føre I, Ólafsson H, Gray SL, Irvine EA, Bovis K, Brown PRA, Swinbank R, Haine T, Lawrence A, Pickart RS, Shapiro M, Woolley A. 2008. The Greenland flow distortion experiment. *Bull. Am. Meteorol. Soc.* **89**: 1307–1324, doi: 10.1175/2008BAMS2508.1.

Renfrew IA, Petersen GN, Sproson DAJ, Moore GWK, Adiwidjaja H, Zhang S, North R. 2009. A comparison of aircraft-based surface-layer observations over Denmark Strait and the Irminger Sea with meteorological analyses and QuikSCAT winds. *Q. J. R. Meteorol. Soc.* **135**: 2046–2066, doi: 10.1002/qj.444.

Rojo M, Claud C, Mallet PE, Noer G, Carleton A, Vicomte M. 2015. Polar low tracks over the Nordic Seas: A 14-winter climatic analysis. *Tellus A* **1**: 1–20.

Shapiro MA, Fedor LS, Hampel T. 1987. Research aircraft measurements of a polar low over the Norwegian Sea. *Tellus A* **39A**: 272–306.

Terpstra A, Michel C, Spengler T. 2016. Forward and reverse shear environments during polar low genesis over the Northeast Atlantic. *Mon. Weather Rev.* **144**: 1341–1354, doi: 10.1175/MWR-D-15-0314.1.

Tourville N, Stephens G, DeMaria M, Vane D. 2015. Remote sensing of tropical cyclones: Observations from CloudSat and A-train profilers. *Bull. Am. Meteorol. Soc.* **96**: 609–622, doi: 10.1175/BAMS-D-13-00282.1.

Wagner JS, Gohm A, Dörnbrack A, Schäfler A. 2011. The mesoscale structure of a polar low: Airborne lidar measurements and simulations. *Q. J. R. Meteorol. Soc.* **137**: 1516–1531, doi: 10.1002/qj.857.

Walters DN, Williams KD, Boutle IA, Bushell AC, Edwards JM, Field PR, Lock AP, Morcrette CJ, Stratton RA, Wilkinson JM, Willett MR, Bellouin N, Bodas-Salcedo A, Brooks ME, Copsey D, Earnshaw PD, Hardiman SC, Harris CM, Levine RC, MacLachlan C, Manners JC, Martin GM, Milton SF, Palmer MD, Roberts MJ, Rodrguez JM, Tennant WJ, Vidale PL. 2014. The Met Office Unified Model global atmosphere 4.0 and JULES global land 4.0 configurations. *Geosci. Model Dev.* **7**: 361–386.

Watanabe SI, Niino H. 2014. Genesis and development mechanisms of a polar mesocyclone over the Japan Sea. *Mon. Weather Rev.* **142**: 2248–2270, doi: 10.1175/MWR-D-13-00226.1.

Wilson DR, Ballard SP. 1999. A microphysically based precipitation scheme for the UK Meteorological Office Unified Model. *Q. J. R. Meteorol. Soc.* **125**: 1607–1636.

Wood N, Staniforth A, White A, Allen T, Diamantakis M, Gross M, Melvin T, Smith C, Vosper S, Zerroukat M, Thuburn J. 2014. An inherently mass-conserving semi-implicit semi-Lagrangian discretization of the deep-atmosphere global non-hydrostatic equations. *Q. J. R. Meteorol. Soc.* **140**: 1505–1520, doi: 10.1002/qj.2235.

Zabolotskikh EV, Mitnik LM, Chapron B. 2013. New approach for severe marine weather study using satellite passive microwave sensing. *Geophys. Res. Lett.* **40**: 3347–3350, doi: 10.1002/grl.50664.

Zappa G, Shaffrey L, Hodges K. 2014. Can polar lows be objectively identified and tracked in the ECMWF operational analysis and the ERA-Interim reanalysis? *Mon. Weather Rev.* **142**: 2596–2608, doi: 10.1175/MWR-D-14-00064.1.

© 2016 The Authors. *Quarterly Journal of the Royal Meteorological Society* published by John Wiley & Sons Ltd on behalf of the Royal Meteorological Society.